Superstructure Controls First Cycle Voltage Hysteresis in O-redox Cathodes

Robert A. House, Urmimala Maitra†, Miguel A. Pérez-Osorio†, Juan G. Lozano, Liyu Jin, James W. Somerville, Laurent C. Duda, Abhishek Nag, Andrew Walters, Kejin Zhou, Matthew R. Roberts, Peter G. Bruce*

Affiliations

Department of Materials, University of Oxford, Parks Road, Oxford, OX1 3PH, UK

Robert A. House, Urmimala Maitra, Miguel A. Perez-Osorio, James W. Somerville, Liyu Jin, Juan G. Lozano, Matthew R. Roberts, Peter G. Bruce

Department of Chemistry, University of Oxford, South Parks Road, Oxford OX1 3QR, UK

Peter G. Bruce

Departamento de Ingeniería y Ciencia de los Materiales y del Transporte, Escuela Técnica Superior de Ingeniería, Universidad de Sevilla, Avenida de los Descubrimientos, 41092, Sevilla (Spain)

Juan G. Lozano

Department of Physics and Astronomy, Division of Molecular and Condensed Matter Physics, Uppsala University, Box 516, S-751 20 Uppsala, Sweden

Laurent C. Duda

Diamond Light Source, Harwell, Oxfordshire, OX11 0DE, UK

Abhishek Nag, Andrew Walters, Kejin Zhou

The Henry Royce Institute, Parks Road, Oxford, OX1 3PH, United Kingdom

Peter G. Bruce

The Faraday Institution, Quad One, Becquerel Avenue, Harwell Campus, Didcot, OX11 0RA, United Kingdom

Peter G. Bruce

†These authors contributed equally

*e-mail: peter.bruce@materials.ox.ac.uk

Alkali-rich transition metal oxide intercalation cathodes can increase the energy density of Li and Na-ion batteries by storing charge on the oxide and transition metal (TM) ions.[1-10] The high voltage associated with oxidation of O^{2-} on the 1st charge is not recovered on discharge, resulting in significantly reduced energy density.[11] Displacement of TM ions from the TM to alkali metal layers has been proposed to explain the 1st cycle voltage loss.[9,12-16] By comparing two closely related intercalation cathodes, $Na_{0.75}[Li_{0.25}Mn_{0.75}]O_2$ and $Na_{0.6}[Li_{0.2}Mn_{0.8}]O_2$, we show that the 1st cycle voltage hysteresis is determined by the superstructure, specifically the local ordering of Li/TM ions in the TM layers. The honeycomb superstructure of $Na_{0.75}[Li_{0.25}Mn_{0.75}]O_2$, present in almost all O-redox compounds, is lost on charging, driven, in part, by formation of molecular O_2 inside the solid. The O_2 molecules are cleaved on discharge reforming O^{2-}, but the Mn ions have migrated in the plane changing the coordination around O^{2-} significantly lowering the voltage on discharge (hysteresis). The ribbon superstructure in $Na_{0.6}[Li_{0.2}Mn_{0.8}]O_2$ inhibits Mn disorder and hence O_2 formation, suppressing hysteresis and promoting stable electron holes on O^{2-} which are revealed by XAS. The results show that voltage hysteresis can be avoided in O-redox cathodes by forming materials with a superstructure (cation ordering) in the TM layers that suppresses TM migration.

During the first charge-discharge cycle, Fig. 1a and 1c, $Na_{0.75}[Li_{0.25}Mn_{0.75}]O_2$ exhibits voltage loss in clear contrast to $Na_{0.6}[Li_{0.2}Mn_{0.8}]O_2$ which does not, despite their very similar compositions. Both materials possess the P2-type structure composed of Na^+ ions in trigonal prismatic (P) coordination and with 2 TMO_2 slabs required to describe the repeat stacking sequence (Fig. 1b). However they exhibit different superstructures, specifically, different ordering of the Li and Mn in the TM layer, (Fig. 1d, 1e). $Na_{0.75}[Li_{0.25}Mn_{0.75}]O_2$ possesses the honeycomb ordering, as observed in the majority of O-redox materials, whereas $Na_{0.6}[Li_{0.2}Mn_{0.8}]O_2$ exhibits a different ordering composed of ribbons of Mn, Extended Data Fig. 2.

Confirmation that both materials are dominated by O-redox was obtained by operando electrochemical mass spectrometry (OEMS) and Mn L-edge x-ray absorption spectroscopy (XAS) along with resonant inelastic x-ray scattering (RIXS). In the case of $Na_{0.75}[Li_{0.25}Mn_{0.75}]O_2$ the data demonstrating that this is an O-redox compound are reported elsewhere, no O-loss was observed.[17] Similarly, for $Na_{0.6}[Li_{0.2}Mn_{0.8}]O_2$, no evidence of O-loss is observed as seen by OEMS, Extended Data Fig. 3. XAS and RIXS identifies electron holes on O, Extended Data Fig. 4.

Honeycomb superstructure lost, ribbon retained

Powder x-ray diffraction (PXRD) data for $Na_{0.6}[Li_{0.2}Mn_{0.8}]O_2$ is presented in Fig. 2b. At the end of charge, the diffraction peaks belonging to the P2 phase have reduced significantly in intensity. New peaks, notably the broad peak at 16.5° in 2θ and peaks at 37° and 66°, have appeared. These peaks correspond to the most prominent peaks indexed on an O2 structure (002, 101 and 110 peaks respectively). Similar changes in the PXRD have been observed for other charged P2-type $Na[TM]O_2$ compounds.[18–22] Upon sufficient desodiation, the TMO_2 slabs glide along a number of unique crystallographic vectors, changing the coordination environment of ions in the alkali metal (AM) layers from trigonal prismatic (P) to octahedral (O), with reduced interlayer spacing. These phases commonly exhibit broad diffraction peaks due to the existence of stacking faults.[18,21,22] The two phase P2 to O2 transition is consistent with the plateau in the electrochemistry observed in Fig. 1c. The changes in the PXRD observed on charging are reversed on discharge, with the crystalline P2-phase being recovered at the end of discharge.

A reduction in peak intensity and peak broadening is also observed in $Na_{0.75}[Li_{0.25}Mn_{0.75}]O_2$ upon charging, Fig. 2a, as is evidence of a new broad peak at around 18° characteristic of O-type layer stacking with a contracted layer spacing, although it is clear that the O-type phase here is not well crystallised as it does not exhibit sharp well defined PXRD peaks. The charging plateau for $Na_{0.75}[Li_{0.25}Mn_{0.75}]O_2$ exhibits a gentle slope, this is consistent with the P2-O2 transition in this case occurring via a continuously evolving intergrowth of O stacking faults in the P structure.

^{6}Li Nuclear Magnetic Resonance (NMR) data (discussed below) is sensitive to all of the Li whether in crystalline or non-crystalline regions and as a result NMR is the best technique to follow changes in Li. For both materials, NMR revealed significant displacement of Li^+ from the TM layer into sites of octahedral coordination in the AM layer upon desodiation, further confirming the presence of O-type stacking faults to accommodate the Li^+ ions. We therefore conclude that transformation from P2 to O-type stacking is near complete in both materials at high states of charge. The PXRD being sensitive to crystalline regions, does not show so clearly the evolution of O2, especially in the case of $Na_{0.75}[Li_{0.25}Mn_{0.75}]O_2$, because the O2 phase is significantly disordered giving rise to fewer diffraction peaks than $Na_{0.6}[Li_{0.2}Mn_{0.8}]O_2$. Interestingly, the diffraction peaks arising from in-plane ordering, as highlighted in Fig. 1, are recovered on discharge for $Na_{0.6}[Li_{0.2}Mn_{0.8}]O_2$ but not significantly for $Na_{0.75}[Li_{0.25}Mn_{0.75}]O_2$.

At the end of charge, the sharp line observed in the ^{6}Li Magic Angle Spinning (MAS) NMR spectrum for Li in the TM layer of pristine $Na_{0.6}[Li_{0.2}Mn_{0.8}]O_2$ disappears and instead a new Li^+ environment with significantly different frequency (centred at 720 ppm, shaded green) appears in its place, Fig 2f. This new shift is in close alignment with those observed for Li^+ in octahedral coordination within AM layers in other layered compounds.[23] It is accordingly assigned to Li residing in the AM layer. After discharge, the new shift disappears and the original shift is reformed with the same, sharp, line shape, indicating the presence of Li again dominantly in their original octahedral TM layer sites. Further NMR data were collected at intermediate states of charge (Extended Data Fig. 5), which confirm that this process occurs via a two-phase mechanism.

The ^{6}Li NMR results for $Na_{0.75}[Li_{0.25}Mn_{0.75}]O_2$, also show that Li^+ is displaced from the TM layers to octahedral sites in the AM layers on charge; an ensemble of shifts centred at 600 ppm is observed in the spectrum for $Na_{0.75}[Li_{0.25}Mn_{0.75}]O_2$ on charge, Fig. 2e. However, on discharge, as the lithium returns to vacancies in the TM layer, a significant broadening of the ensemble of isotropic chemical shifts centred around 1800 ppm is observed. This is indicative of a range of new Li environments generated from different local ordering of Mn. This is in stark contrast to the ribbon superstructure ordering of $Na_{0.6}[Li_{0.2}Mn_{0.8}]O_2$, which does not change and therefore provides the same sites for Li^+ as were present in the pristine material, i.e. TM ordering is largely retained in $Na_{0.6}[Li_{0.2}Mn_{0.8}]O_2$ but not in $Na_{0.75}[Li_{0.25}Mn_{0.75}]O_2$. This is evidence that Mn is mobile in honeycomb ordered $Na_{0.75}[Li_{0.25}Mn_{0.75}]O_2$. Integration of the Li signals for both materials shows that any loss of Li from the structure is < 1% (i.e. below the limit of detection) and all of the Li that is displaced returns to the TM layers. This also confirms that Na^+, not Li^+, is the dominant species removed and reinserted into the structure on charge/discharge.

Annular dark field - scanning transmission electron microscopy (ADF-STEM) data indicate that the honeycomb superstructure of the pristine $Na_{0.75}[Li_{0.25}Mn_{0.75}]O_2$ is almost entirely lost after charging to 4.5 V. Viewing along the [010] direction, Fig. 2c, the 2-atom (Mn-Mn) dumbbells are less clearly resolved in most parts of the image after charging to 4.5 V, indicating loss of the in-plane order. After discharge to 2 V, there is virtually no periodic variation in contrast along the layers showing the honeycomb is completely lost. In contrast to this, the ADF-STEM image of $Na_{0.6}[Li_{0.2}Mn_{0.8}]O_2$ along the [010] direction shows striking retention of the 4-atom (Mn-Mn-Mn-Mn) configuration associated with the ribbon ordering described in Fig. 1e, with some slight disorder evident at the end of discharge. These results are in agreement with the PXRD and NMR data showing predominantly O-type stacking in both cases. Further images from different regions of each cycled sample are included in Extended Data Fig. 6 showing more comprehensively the structural changes. It is important to note that PXRD and NMR, unlike STEM, sample the whole material, therefore the STEM results are representative of the material as a whole; the consistency between all three techniques reinforces the interpretation of the results.

Together the NMR, PXRD and STEM data shows that the honeycomb superstructure is unstable on charging. Li^+ is displaced to the AM layers and irreversible in-plane migration of Mn results in a more disordered arrangement of Mn and vacancies in the TM layer in the charged state of $Na_{0.75}[Li_{0.25}Mn_{0.75}]O_2$. The honeycomb ordering is not recovered on discharge, with the consequence that the Li ions return to different sites in the TM layer. In contrast, for the ribbon superstructure in $Na_{0.6}[Li_{0.2}Mn_{0.8}]O_2$, the ordering remains predominantly unchanged and the high voltage on charge is retained on discharge.

Molecular O_2 or stable e^- holes

Density functional theory (DFT) calculations were performed on structural models of the charged state, O2-$Na_0Li_{0.25}Mn_{0.75}O_2$, with Li^+ in the AM layer, vacancies in the TM layer and different in-plane configurations of Mn. As shown in Extended Data Fig. 7a, a large number of configurations appear to be very similar in energy to the honeycomb arrangement (within ~20-30 meV/f.u., comparable to the thermal energy, kT = 25.7 meV) with one notable exception that was significantly (225 meV/f.u.) lower in energy. In this arrangement, TM vacancies cluster together resulting in replacement of the oxygens coordinated by 2 Mn (O-Mn_2) which occurs for all O in the honeycomb structure, with O coordinated by 3 Mn (O-Mn_3) and O atoms completely decoordinated from Mn, which dimerise with 1 other O bonded to 1 Mn. The O-O bond length is 1.2 Å (directly comparable to that of molecular O_2 = 1.208 Å) and the Mn-O distance is 2.2 Å, consistent with a weak Mn-O bond and hence formation of a Mn-η^1-O_2 moiety containing molecular O_2. The dimerisation of O to form Mn-η^1-O_2 lowers the overall energy of the charged structure and drives the TM migration.

To evaluate what impact this structural change has on the discharge voltage, we calculated this quantity directly using the computed energies of the charged and discharged structures. To model the discharged state, the Mn and vacancy arrangement corresponding to the deep energy minimum described above was retained and the AM and TM layer vacancy cluster repopulated with Na^+ and Li^+ respectively. The resulting relaxed structure no longer possessed the short O-O distance (now 2.6 Å); the O-O bond of molecular O_2 is cleaved on discharge and fully reduced O^{2-} formed, Extended Data Fig. 6c. A value of 3.2 V was obtained from the calculation of the discharge voltage, in good agreement with that observed from the electrochemistry, Fig. 1a, supporting the

structural models obtained from DFT. We considered a range of other Mn disordered structures and all were higher in energy than the vacancy cluster reported here. Also the other disordered configurations could not produce a voltage as close to the experimentally observed voltage. Similar voltage calculations were carried out for the ribbon structure, $Na_{0.6}[Li_{0.2}Mn_{0.8}]O_2$, where, assuming no change in in-plane ordering occurs, a value of 4.1 V is obtained in close agreement with the observed discharge plateau.

To explore experimentally the nature of the oxidised oxygen species on charge, RIXS spectroscopy, but of a higher resolution than in past studies, was employed.[4,12,19,24-27] Our data reveal the underlying fine structure of the elastic peak, labelled B in Fig. 3a, and show that it is composed of a progression of energy loss peaks associated with the vibrations of the O-O bond and with a fundamental vibrational frequency of ~1600 cm^{-1}, Fig. 3d, closely matching that of molecular O_2, Fig. 3b. Together with the broad inelastic peak, A, these features bear strong resemblance to the RIXS spectrum for gaseous molecular O_2, Fig. 3b.[28] The ultra high vacuum conditions under which RIXS measurements are made ensures that the electrode materials are fully 'out-gassed' and hence O_2 molecules in the gas phase or surface adsorbed cannot account for the RIXS observations, supporting O_2 bound with η^1 coordination to Mn. Furthermore, both spectroscopic features A and B no longer appear in the discharged sample, indicating that the O_2 species is reduced on discharge.

Oxidation of O^{2-} results in oxygen species with an electronic driving force for O dimerization. This is reflected in the observation of molecular O_2 here and reports of peroxo-like (O_2^{n-}) with O-O bond lengths of 1.4-2.5 Å in 4d- and 5d-based materials by Tarascon and others.[6,8,29,30] Here we see clear evidence that molecular O_2 (O-O 1.2 Å) forms and not O_2^{2-} (O-O 1.5 Å) or peroxo-like species (O-O 1.9-2.5 Å). This is the first time, as far as we are aware, that molecular O_2 has been observed in the bulk of O-redox materials and their important role in O-redox, in particular their role in voltage hysteresis, revealed. This bulk O_2 is trapped in the vacancy clusters and has no mechanism of diffusing through the material to the surface, however, any O_2 that is formed at the surface can escape. Although no direct O_2 loss is seen for either $Na_{0.6}[Li_{0.2}Mn_{0.8}]O_2$ or $Na_{0.75}[Li_{0.25}Mn_{0.75}]O_2$, some CO_2 is observed in both cases across the charging plateaux. It has been shown that singlet O_2 is typically evolved from O-redox materials and it reacts with the electrolyte forming CO_2.[31,32] If O_2 release is forced to be fast, by for example stepping to a high potential, a small amount of O_2 can be detected.[17]

A small signature from molecular O_2 is also seen in the RIXS for ribbon ordered $Na_{0.6}[Li_{0.2}Mn_{0.8}]O_2$ at the end of charge. This is in accord with the electrochemical data and ADF-STEM images that show the ribbon structure of $Na_{0.6}[Li_{0.2}Mn_{0.8}]O_2$ is not completely preserved during the 1st cycle and some low voltage capacity is seen on the first discharge. However, turning to the O K-edge XAS data presented in Fig. 3c, in addition to the O_2 feature appearing at 531 eV, there is also a new, unique feature appearing before the pre-edge at 527.5 eV. This feature is exactly where electron hole states lying just above the fermi energy would be expected to appear and hence represent electronic states on O that can be reduced at high potential (i.e. O-redox without voltage hysteresis). This is the first evidence, as far as we know, of true, stable electron holes on O^{2-} and is distinct from the localised holes that form on O_2.

Superstructure controls voltage hysteresis

Hysteresis in O-redox materials has been related to the number of electron holes formed on oxygen, with too many resulting in structural instability and voltage loss.[34] However, there are a number of materials that are less oxidised than ribbon $Na_{0.6}[Li_{0.2}Mn_{0.8}]O_2$ (0.2 electron holes, h^+, per O) yet still exhibit hysteresis such as Na_2RuO_3 (0.13 h^+ per O) and $Li[Ni_{1/3}Li_{1/9}Mn_{5/9}]O_2$ (0.13 h^+ per O).[1,10] The crucial difference here is that the latter examples both possess honeycomb ordered TM layers, like $Na_{0.75}[Li_{0.25}Mn_{0.75}]O_2$, whereas the former exhibits ribbon ordering. Further examination of the literature reveals a strong evidential link between superstructure ordering and voltage hysteresis which extends across P2 and P3 Na-ion compounds and Li-rich O3 structures. Honeycomb ordering is exhibited by the vast majority of layered O-redox cathodes which all consistently exhibit voltage hysteresis and the only known examples without voltage hysteresis have a different ordering scheme. P3-$Na_{0.6}[Li_{0.2}Mn_{0.8}]O_2$, has the same ribbon ordering scheme as P2-$Na_{0.6}[Li_{0.2}Mn_{0.8}]O_2$, but with a different stacking sequence, as we show in the Extended Data 8, and does not exhibit voltage hysteresis. $Na_2Mn_3O_7$, which has a unique in-plane ordering scheme corresponding to its $[\square_{1/7}Mn_{6/7}]$ TM layer composition, also shows no voltage hysteresis.[14,15,35]

The highest energy O 2p states in pristine honeycomb $Na_{0.75}[Li_{0.25}Mn_{0.75}]O_2$ and ribbon $Na_{0.6}[Li_{0.2}Mn_{0.8}]O_2$ are those coordinated by two ionic cations (Li^+, Na^+) from the TM and AM layer respectively, forming Na^+-O2p-Li^+ dumbells.[4,5] On charging, electrons are removed from these states oxidising O^{2-} to form O^{n-} (n<2) and triggering displacement of Li^+ from the TM to AM layers, Fig. 4b. For perfect honeycomb ordering, all oxide ions are coordinated in the TM layer by 2 Mn, O-Mn_2, they are degenerate in energy and equally susceptible to oxidation on charging. However, this degeneracy can be broken through Mn migration which changes the Mn coordination of the O^{n-} ions from O-Mn_2 to: more coordinated O-Mn_3, less coordinated O-Mn_1, and uncoordinated O (O-Mn_0), Fig. 4a. The unbonded O (O-Mn_0) is stabilised by dimerising with the O-Mn_1 forming the Mn-η^1-O_2 moieties, as demonstrated by DFT and RIXS above. It is this electronic driving force that promotes Mn migration to disrupt the honeycomb superstructure. Discharge involves reduction of the unoccupied states on O_2, triggering cleavage of the O-O bond, the formation of fully reduced O^{2-} and the return of Li^+ to the TM layers. However, now they return to different sites, instead occupying sites in the vacancy cluster. The Na^+ ions return to the AM layers. The discharge voltage for this process (3.2 V, as noted above) is significantly lower than the voltage on charge, explaining the first cycle voltage hysteresis of the honeycomb superstructured O-redox cathode. In the case of the ribbon superstructure, Mn migration is suppressed preventing O_2 formation and stabilising electron holes on O^{2-}, Fig. 3c, 4c. In the charged honeycomb structure, only 2 Mn are required to migrate into adjacent vacancies to generate free O^{2-} that can pair with a neighbouring O to form O_2, Fig. 5a. In contrast, since vacancies are more dispersed in the ribbon structure, multiple Mn displacements, including sequental Mn hops would be required to form the TM vacancy clusters, Fig. 5b. Ribbon ordering thus provides increased stability for high voltage O redox (4.1 V from calculation) by preserving the degeneracy of the O 2p states.

Ribbon ordering is not, however, 100% stable. Even on the first cycle not all the charge capacity at 4.3 V is recovered on discharge. Furthermore, Extended Data Fig. 9 shows that dwelling for increasing time in the highly desodiated charged state promotes the loss of the high voltage discharge, suggesting increased Mn migration. Upon extended cycling the discharge plateaux gradually decrease in length with greater evidence of low voltage capacity similar to that of $Na_{0.75}[Li_{0.25}Mn_{0.75}]O_2$. PXRD data (Extended Data Fig. 10) confirm that after 10 cycles the diffraction peaks arising from the superstructure ordering are reduced and there is increasing strain broadening within the ab plane indicative of Mn migration and loss of the ribbon ordering. ADF-STEM imaging (Extended Data Fig. 6) also shows loss of ribbon ordering after 10 cycles. The loss of voltage correlates with the loss of superstructure further reinforcing the relationship between the two. This irreversibility of the high voltage plateau is also seen for the P3-type analogue of P2-$Na_{0.6}[Li_{0.2}Mn_{0.8}]O_2$[14,15] which exhibits the same ribbon superstructure ordering.

Although ribbon ordering is not completely stable, a compound possessing an ordering scheme with even more dispersed vacancy ordering has been reported which shows even higher reversiblity of the high voltage O-redox plateau, Fig. 5c.[35] This observation, underpinned by our work exposing the critical role of superstructure in preserving high voltage O-redox, defines a compelling new strategy in the search for high energy density Li-rich cathodes.

References

1. Lu, Z., Beaulieu, L. Y., Donaberger, R. A., Thomas, C. L. & Dahn, J. R. Synthesis, Structure, and Electrochemical Behavior of Li[NixLi1/3−2x/3Mn2/3−x/3]O2. J. Electrochem. Soc. 149, A778 (2002).

2. Johnson, C. S. et al. The significance of the Li2MnO3 component in 'composite' xLi2MnO3·(1−x)LiMn0.5Ni0.5O2 electrodes. Electrochem. commun. 6, 1085–1091 (2004).

3. Koga, H. et al. Reversible Oxygen Participation to the Redox Processes Revealed for Li1.20Mn0.54Co0.13Ni0.13O2. J. Electrochem. Soc. 160, A786–A792 (2013).

4. Luo, K. et al. Charge-compensation in 3d-transition-metal-oxide intercalation cathodes through the generation of localized electron holes on oxygen. Nat. Chem. 8, 684–691 (2016).

5. Seo, D.-H. et al. The structural and chemical origin of the oxygen redox activity in layered and cation-disordered Li-excess cathode materials. Nat. Chem. 8, 692–697 (2016).

6. Saubanère, M., McCalla, E., Tarascon, J.-M. & Doublet, M.-L. The intriguing question of anionic redox in high-energy density cathodes for Li-ion batteries. Energy Environ. Sci. 9, 984–991 (2016).

7. Oishi, M. et al. Direct observation of reversible oxygen anion redox reaction in Li-rich manganese oxide, Li2MnO3, studied by soft X-ray absorption spectroscopy. J. Mater. Chem. A 4, 9293–9302 (2016).

8. Sathiya, M. et al. Reversible anionic redox chemistry in high-capacity layered-oxide electrodes. Nat. Mater. 12, 827–835 (2013).

9. Hong, J. et al. Metal–oxygen decoordination stabilizes anion redox in Li-rich oxides. Nat. Mater. 18, 256–265 (2019).

10. Mortemard de Boisse, B. et al. Intermediate honeycomb ordering to trigger oxygen redox chemistry in layered battery electrode. Nat. Commun. 7, 11397 (2016).

11. Lu, Z. & Dahn, J. R. Understanding the Anomalous Capacity of Li/Li[NixLi(1/3−2x/3)Mn(2/3−x/3)]O2 Cells Using In Situ X-Ray Diffraction and Electrochemical Studies. J. Electrochem. Soc. 149, A815 (2002).

12. Gent, W. E. et al. Coupling between oxygen redox and cation migration explains unusual electrochemistry in lithium-rich layered oxides. Nat. Commun. 8, (2017).

13. Croy, J. R. et al. First-charge instabilities of layered-layered lithium-ion-battery materials. Phys. Chem. Chem. Phys. 17, 24382–24391 (2015).

14. Du, K. et al. Exploring Reversible Oxidation of Oxygen in a Manganese Oxide. Energy Environ. Sci. 6, 3–5 (2016).

15. Rong, X. et al. Structure-Induced Reversible Anionic Redox Activity in Na Layered Oxide Cathode. Joule 2, 125–140 (2018).

16. Pearce, P. E. et al. Evidence for anionic redox activity in a tridimensional-ordered Li-rich positive electrode β-Li2IrO3. Nat. Mater. 16, 580–586 (2017).

17. House, R. A. et al. What Triggers Oxygen Loss in Oxygen Redox Cathode Materials? Chem. Mater. 31, 3293–3300 (2019).

18. Yabuuchi, N. et al. A new electrode material for rechargeable sodium batteries: P2-type Na2/3[Mg0.28Mn0.72]O2 with anomalously high reversible capacity. J. Mater. Chem. A 2, 16851–16855 (2014).

19. Maitra, U. et al. Oxygen redox chemistry without excess alkali-metal ions in Na2/3[Mg0.28Mn0.72]O2. Nat. Chem. 10, 288–295 (2018).

20. Tournadre, F. et al. On the mechanism of the P2–Na0.70CoO2→O2–LiCoO2 exchange reaction—Part I: proposition of a model to describe the P2–O2 transition. J. Solid State Chem. 177, 2790–2802 (2004).

21. Lu, Z. & Dahn, J. R. In Situ X-Ray Diffraction Study of P2-Na2/3[Ni1/3Mn2/3]O2. J. Electrochem. Soc. 148, A1225 (2001).

22. Tournadre, F., Croguennec, L., Willmann, P. & Delmas, C. On the mechanism of the P2-Na0.70CoO2→O2- LiCoO2 exchange reaction - Part II: An in situ X-ray diffraction study. J. Solid State Chem. 177, 2803–2809 (2004).

23. Clément, R. J. et al. Direct evidence for high Na+ mobility and high voltage structural processes in P2-Nax[LiyNizMn1-y-z]O2 (x, y, z ≤ 1) cathodes from solid-state NMR and DFT calculations. J. Mater. Chem. A 5, 4129–4143 (2017).

24. House, R. A. et al. Lithium manganese oxyfluoride as a new cathode material exhibiting oxygen redox. Energy Environ. Sci. 11, 926–932 (2018).

25. Wu, J. et al. Fingerprint Oxygen Redox Reactions in Batteries through High-Efficiency Mapping of Resonant Inelastic X-ray Scattering. Condens. Matter 4, 5 (2019).

26. Xu, J. et al. Elucidating anionic oxygen activity in lithium-rich layered oxides. Nat. Commun. 9, (2018).

27. Yang, W. & Devereaux, T. P. Anionic and cationic redox and interfaces in batteries: Advances from soft X-ray absorption spectroscopy to resonant inelastic scattering. J. Power Sources 389, 188–197 (2018).

28. Arhammar, C. et al. Unveiling the complex electronic structure of amorphous metal oxides. Proc. Natl. Acad. Sci. 108, 6355–6360 (2011).

29. McCalla, E. et al. Visualization of O-O peroxo-like dimers in high-capacity layered oxides for Li-ion batteries. Science 350, 1516–21 (2015).

30. Xie, Y., Saubanère, M. & Doublet, M.-L. Requirements for reversible extra-capacity in Li-rich layered oxides for Li-ion batteries. Energy Environ. Sci. 10, 266–274 (2017).

31. Wandt, J., Freiberg, A. T. S., Ogrodnik, A. & Gasteiger, H. A. Singlet oxygen evolution from layered transition metal oxide cathode materials and its implications for lithium-ion batteries. Mater. Today 21, 825–833 (2018).

32. Freiberg, A. T. S., Roos, M. K., Wandt, J., de Vivie-Riedle, R. & Gasteiger, H. A. Singlet Oxygen Reactivity with Carbonate Solvents Used for Li-Ion Battery Electrolytes. J. Phys. Chem. A 122, 8828–8839 (2018).

33. Radjenovic, P. M. & Hardwick, L. J. Evaluating chemical bonding in dioxides for the development of metal–oxygen batteries: vibrational spectroscopic trends of dioxygenyls, dioxygen, superoxides and peroxides. Phys. Chem. Chem. Phys. 21, 1552–1563 (2019).

34. Ben Yahia, M., Vergnet, J., Saubanère, M. & Doublet, M.-L. Unified picture of anionic redox in Li/Na-ion batteries. Nat. Mater. 18, 496–502 (2019).

35. Mortemard de Boisse, B. et al. Highly Reversible Oxygen-Redox Chemistry at 4.1 V in Na4/7−x[□1/7Mn6/7]O2 (□: Mn Vacancy). Adv. Energy Mater. 8, 1800409 (2018).

Acknowledgements

PGB is indebted to the EPSRC, including the SUPERGEN programme, the Henry Royce Institute for Advanced Materials [EP/R00661X/1, EP/S019367/1, EP/R010145/1] and the Faraday Institution [FIRG007, FIRG008] for financial support. We would like to thank Dr Helen Playford and Dr Ron Smith at ISIS, Harwell Campus for collecting Neutron Diffraction data. Support from the EPSRC (EP/K040375/1 'South of England Analytical Electron Microscope') is also gratefully acknowledged. The authors would like to acknowledge the use of the University of Oxford Advanced Research Computing (ARC) facility in carrying out this work. http://dx.doi.org/10.5281/zenodo.22558, and the resources provided by the Cambridge Tier-2 system operated by the University of Cambridge Research Computing Service (http://www.hpc.cam.ac.uk) funded by EPSRC Tier-2 capital grant EP/P020259/1, via the Advanced Materials for Alkali-ion Batteries (AMAiB) project. Synchrotron radiation experiments were performed at i21 beamline, Diamond Light Source, Harwell with supporting data collected from the ADRESS beamline, Swiss Light Source, Villigen, Switzerland and BL27SU, Spring8, Japan. We acknowledge technical and experimental support at the ADRESS beamline by T. Schmitt, D. McNally, X. Lu, L. Nue and M. Dantz and at BL27SU beamline by K. Tsuruta. We would like to thank Dr Nick Rees, Dept. of Chemistry, Oxford University for help collecting NMR spectra.

Author Information

Author Contributions

R.A.H., U.M., M.R.R. and P.G.B. conceived the study. U.M. and R.A.H. carried out the materials synthesis, characterisation and testing. R.A.H., U.M., J.W.S., M.R.R., L.C.D., contributed to the measurement processing and interpretation of the spectroscopic data. M.A.P-O. performed the DFT calculations. L.J. collected, processed and interpreted the NMR data. J.G.L. performed and interpreted the ADF-STEM measurements. R.A.H., A.N., A.W. and K.Z. performed high resolution RIXS and sXAS measurements. R.A.H. and P.G.B. wrote the manuscript with contributions and revisions from all authors.

Competing Interests

The authors declare no competing interests

Materials & Correspondence

Correspondence to Peter G. Bruce

FIGURE LEGENDS

Figure 1. Electrochemistry and Structure of Honeycomb and Ribbon Ordered Cathode Materials 1st cycle voltage curves for (a) $Na_{0.75}[Li_{0.25}Mn_{0.75}]O_2$ and (c) $Na_{0.6}[Li_{0.2}Mn_{0.8}]O_2$. As discussed in the text, the dominant species extracted on charge is Na^+ not Li^+. 2.0 V discharge and 4.5 V charge limits. Rate 10 mA g^{-1}. (b) Structural model of P2-type $Na[TM]O_2$ with no in-plane ordering; space group $P6_3/mmc$. Oxide layers stack in ABBA sequence giving alkali metal (AM) layers of trigonal prismatic Na^+ sandwiched between transition metal (TM) layers of octahedral Mn partially substituted with Li. (d) $Na_{0.75}[Li_{0.25}Mn_{0.75}]O_2$ possesses the P2 structure with the well-known honeycomb superstructure ordering of Li and Mn within the TM layer; space group $P6_3$. 2-atom dumbbells (Mn-Mn) along the [010] direction characteristic of the honeycomb superstructure are seen with ADF-STEM. Note that the honeycomb superstructure dominates although the composition is not that of the ideal honeycomb ($Li_{1/3}Mn_{2/3}$). (e) $Na_{0.6}[Li_{0.2}Mn_{0.8}]O_2$ possesses the same P2 structure but with superstructure ordering of Li and Mn within the TM layer instead forming ribbons. This superstructure ordering gives rise to unique diffraction peaks in the PXRD pattern (highlighted blue) and can be fully indexed to the P21/c space group, see Extended Data Fig. 2. It also gives rise to 4-atom dumbbells (Mn-Mn-Mn-Mn) when viewed along the [010] direction, as observed in the ADF-STEM images.

Figure 2. Evidence for the Loss of Honeycomb Ordering and Retention of Ribbon Ordering on the 1st Cycle (a) and (b), PXRD data for honeycomb ordered P2-$Na_{0.75}[Li_{0.25}Mn_{0.75}]O_2$ and ribbon ordered P2-$Na_{0.6}[Li_{0.2}Mn_{0.8}]O_2$ respectively: pristine, after charging to 4.5V and discharging to 2V. Insets highlight the superstructure peak region. Superstructure peaks corresponding to the ribbon ordering reappear on discharge indicating retention of in-plane ordering whereas for the honeycomb the superstructure peak at 22° is lost irreversibly. (c) and (d), STEM-ADF images. Projections are parallel to the ab plane along [010] zone-axis. Light and dark contrast corresponds to the heavier (Mn) and lighter (Li, Na and O) scattering respectively. The ribbon superstructure is retained in the case of $Na_{0.6}[Li_{0.2}Mn_{0.8}]O_2$ on charge and discharge, although there is some evidence of disorder in the discharged state, which is discussed in the text. In contrast, the 2 atom (Mn-Mn) dumbbells within the TM layers almost completely disappear showing honeycomb ordering is lost. There is some evidence of scattering between the TM layers in the charged honeycomb structure which might indicate some displacement of Mn into the AM layers, but the dominant Mn disorder is in-plane. (e) and (f) ^6Li MAS NMR data. Peaks corresponding to the isotropic shifts for Li in the TM layers, Li_{TM}, are shown in purple and those corresponding to Li in AM layers, Li_{AM}, are shown in green. All other peaks are spinning sidebands. For ribbon ordered $Na_{0.6}[Li_{0.2}Mn_{0.8}]O_2$, lithium migrates from TM to AM layers on charging and this is reversed on discharge. For honeycomb ordered $Na_{0.75}[Li_{0.25}Mn_{0.75}]O_2$, lithium again migrates from TM to AM layers on charging, however on discharge, Li

repopulates a TM layer with different local ordering as a result of Mn migration, labelled Li_{TM}*. Small amounts of Li_2MnO_3 and Li-containing diamagnetic impurities are shaded in black and red, respectively.

Figure 3. Spectroscopic Evidence for O_2 Formation and Stable Electron Holes on O^{2-} O K-edge XAS and high resolution RIXS spectra recorded at an excitation energy of 531 eV for (a) honeycomb ordered $Na_{0.75}[Li_{0.25}Mn_{0.75}]O_2$ and (c) ribbon ordered $Na_{0.6}[Li_{0.2}Mn_{0.8}]O_2$ in the pristine, charged (4.5 V), and discharged (2 V) states. The red highlighted pre-edge feature at 531 eV and RIXS features A and B are characteristic of O-redox. With high resolution RIXS, Feature B is resolved into a progression of energy loss peaks, (d), arising from the vibrations of the O-O bond with a fundamental vibrational frequency of ~1600 cm^{-1} matching that of molecular O_2 and that expected from the 1.2 Å O-O bond in the Mn-η^1-O_2 species predicted from DFT. The high resolution RIXS spectrum for molecular O_2 at 530.3 eV (†reproduced with permission from C. Arhammar et al.[28]) is shown in (b) and literature values for the bond lengths and frequencies of O-O dimers for comparison in (e).[33] The O K-edge XAS spectrum for ribbon ordered $Na_{0.6}[Li_{0.2}Mn_{0.8}]O_2$ in the charged state shows the formation of stable electron holes (h^+) on O^{2-} (green) at low energy (high voltage).

Figure 4. Electronic and Structural Changes Accompanying O-redox (a) Density of States (DoS) plots from DFT for honeycomb ordered $Na_{0.75}[Li_{0.25}Mn_{0.75}]O_2$ at different states of charge. Pristine state: honeycomb ordering with frontier Na^+-O2p-Li^+ oxygen states that are oxidised on charge. Charged state: Li sites in the TM layer are vacant, in-plane migration of Mn (along arrows) forms vacancy clusters triggered by formation of molecular O_2 (1.2 Å). Electron holes localise in molecular π^* spin down states of O_2, represented by red shading in the DoS. Discharged structure: Electrons populate the anti-bonding π^* and σ^* states breaking the O-O bond and forming 2 O^{2-} (2.6 Å apart). These oxide ions are surrounded by alkali ions in the structure and thus are at the top of valence band (purple in DoS). (b) Layer stacking at different states of charge for both $Na_{0.75}[Li_{0.25}Mn_{0.75}]O_2$ and $Na_{0.6}[Li_{0.2}Mn_{0.8}]O_2$. (c) DoS plots from DFT for ribbon ordered $Na_{0.6}[Li_{0.2}Mn_{0.8}]O_2$. Pristine state: There are two unique O environments O-Mn_2 (blue) and O-Mn_3 (green). Charged state: Electron holes localise on O-Mn_2 close to the bottom of the conduction band, blue in DoS. Discharged state: Ribbon ordering maintained, structure unchanged from pristine. In all DoS plots, the Fermi energy level is set to zero.

Figure 5. Dependence of O-redox Stability on Superstructure In plane Mn migrations (arrows) required to form O_2 molecules (orange ellipses) in the TM layer of charged (a) honeycomb, (b) ribbon and (c) mesh arrangements. More Mn migrations are required to form O_2 in the ribbon and mesh structures and Mn must migrate into sites already filled by Mn making O_2 formation less likely. TM layer vacancies are represented by □.

Methods

Synthesis $Na_{0.6}[Li_{0.2}Mn_{0.8}]O_2$ and $Na_{0.75}[Li_{0.25}Mn_{0.75}]O_2$ were prepared via solid state-reaction between stoichiometric amounts of Na_2CO_3 (≥99.0%, Aldrich), Li_2CO_3 (≥99.0%, Aldrich), and MnO_2 (≥99.0%, Aldrich). The precursors were ball-milled for 1 h using a Retsch PM100, pressed into pellets and calcined at 800°C for 12 h under flowing oxygen. Heating and cooling was conducted under a controlled rate of 10°C min^{-1} in both cases except for $Na_{0.6}[Li_{0.2}Mn_{0.8}]O_2$ which was cooled at 2°C min^{-1}. As prepared materials were transferred into an inert Ar atmosphere without exposure to air and stored for characterisation. All subsequent procedures were carried out without exposure to air.

Structural Characterisation X-ray Powder Diffraction Patterns were collected using a Cu source Rigaku diffractometer. Neutron Powder Diffraction Patterns were collected at the POLARIS diffractometer at the ISIS neutron source. Powders were loaded into Vanadium canisters and sealed under inert atmosphere for measurement. Reitveld profile refinements were performed using the GSAS suite of programs.

Electrochemical Characterisation Electrodes were prepared by mixing 80 wt.% active material, 10 wt.% Super P carbon and 10 wt.% Polytetrafluoroethylene (PTFE) binder in a mortar and pestle and rolling to form a self-standing film. Electrodes were incorporated into CR2032 coin cells with electrolyte-soaked ($NaPF_6$ (Kishida) in

propylene carbonate (99.7%, Sigma)) Whatman™ glass fibre separators and Na metal counter electrodes. Galvanostatic charge-discharge was carried out at a rate of 10 mA g^{-1} using a Maccor Series 4000.

Operando Electrochemical Mass Spectrometry was carried out using a cell (ECC-Std from EL-CELL) with gas inlet and outlet ports. Ar carrier gas was flowed at constant rate (0.8 µL min^{-1} Bronkhurst mass-flow controller) through the cell and into a quadrupole mass spectrometer (Thermo Fischer) equipped with turbomolecular pump (Pfeiffer Vacuum).

Solid-state NMR experiments were performed on a 400 MHz Bruker Avance III HD spectrometer at the ^{6}Li Larmor frequency of 58.99 MHz. All spectra were recorded with a rotor-synchronised Hahn-echo pulse sequence. The ^{6}Li spectra were externally referenced with LiCl aqueous solution at 0.0 ppm.

For $Na_{0.6}[Li_{0.2}Mn_{0.8}]O_2$, a 3.2mm magic angle spinning (MAS) probe was used and the MAS rate was 19 kHz and the probe temperature was controlled at 268 K. The applied π/2 pulse length was 3.5 μs and the delay between π/2 and π pulses were 47.4 μs (1 rotor period). The transmitter frequency was set to 1600 ppm. For $Na_{0.75}[Li_{0.25}Mn_{0.75}]O_2$, a 1.9mm MAS probe was used with the MAS rate of 38 kHz and the probe temperature was set to 298 K. The applied π/2 pulse length was 2 μs and the delay between π/2 and π pulses were 23.3 μs (1 rotor periods). The transmitter frequency was set to 1600 ppm.

The spectra were normalized by the total number of scans and the weight of active materials packed in the rotors. Spectra fitting and deconvolution were carried out by the dmfit program.[36]

ADF-STEM micrographs were collected on an aberration corrected JEOL ARM 200F operated at 200 kV. The convergence semi-angle used was 22 mrad, and the collection semi-angle was 69.6-164.8 mrad (ADF). In all cases, sets of fast-acquisition multi-frame images were recorded and subsequently corrected for drift and scan distortions using SmartAlign.[37]

Computation Density functional theory (DFT) calculations including Hubbard corrections[38] were performed using Quantum Espresso.[39] We employed the Perdew, Burke and Ernzerhof (PBE)[40] exchange-correlation functional. The core-valence interaction was taken into account by using the projector augmented wave (PAW) method.[41] The wavefunctions were represented through plane-wave basis set with an energy cutoff of 70 Ry. Spin polarization was included. All calculations were performed considering a ferromagnetic ordering of Mn atoms. A Hubbard U parameter of 4 eV for Mn 3d states was used, similar to that reported for other closely related compounds.[6,42] To find the k-point condition, the total energy of the supercell was converged with respect to the number of k points, and convergence was reached with a 2x2x2 Monkhorst-Pack k-point grid. Crystal structures were relaxed until forces on the atoms were less than 0.08 eV/Angstrom and the total stresses on the cell were less than 0.05 kBar. The supercell for $Na_{0.75}[Li_{0.25}Mn_{0.75}]O_2$ contains 90 atoms: 18 Na atoms; 6 Li atoms; 18 Mn atoms; and 48 O atoms.

For electronic structure calculations, we carried out spin-polarized density functional theory (DFT) calculations employing the HSE functional. An exact exchange mixing parameter of 0.25 was used for all calculations. Norm-conserving pseudopotentials were used to describe the core-valence interaction.[43] The electronic wavefunctions were described using a plane-wave basis set with an energy cutoff of 80 Ry. A Monkhorst-Pack k-point grid of 2 × 2 × 2 was used. The input structures were obtained from the DFT+U lattice relaxations, and the nuclear positions were allowed to further relax at the HSE level, keeping the lattice parameters fixed.

Intercalation-deintercalation voltages (V) were computed using the Nernst equation:

$$V = -\frac{\Delta G}{zF}$$

where ΔG is the Gibbs free energy change, F is the Faraday constant and z is the charge that is transferred. The change in the Gibbs free energy is defined as ΔG=ΔE+PΔV-TΔS, where P and T are pressure and temperature, respectively, and ΔE, ΔV and ΔS are the change in internal energy, volume and entropy, respectively. The first-principles calculations were carried out at 0 K and zero pressure. Under these conditions, the Gibbs free energy

change is then given by the change in the internal energy, ΔG=ΔE. Thus, for the sodium deintercalation-intercalation reaction $Na_{x1}TmO_2 \rightarrow Na_{x2}TmO_2 + (x_1\text{-}x_2)$ Na, the voltage is given by:

$$V = -\frac{E(Na_{x1}TmO_2) - E(Na_{x2}TmO_2) - (x_1 - x_2)E(Na)}{(x_2 - x_1)F}$$

where $x_1 > x_2$ and $E(Na_{x1}TmO_2)$ and $E(Na_{x2}TmO_2)$ are the internal energies of the sodiated and desodiated transition metal (Tm) oxides, respectively, and E(Na) is the internal energy of metallic sodium. These quantities are obtained directly from the first principles calculations. This procedure is well established.[44,45]

For phases with partial Na occupancy, Na ordering was investigated using combinatorics. Simple random sampling (SRS) was used to choose a representative subset of non-symmetry equivalent configurations for relaxation. A similar methodology was employed to investigate Mn disorder in the charged honeycomb phase. Fully desodiated models were prepared for the charged phases to make calculations more computationally tractable.

Spectroscopic Characterisation Soft x-ray absorption spectroscopy (XAS) and high resolution resonant inelastic x-ray scattering (RIXS) data were recorded at i21 Diamond Light Source in the UK with supporting data from BL27SU of the RIKEN/JASRI Spring8 synchrotron in Japan and the ADRESS beamline at the Swiss Light Source. Mn L-edge data were collected in inverse partial fluorescence yield mode (iPFY), O K-edge data are plotted in the partial fluorescence yield mode (PFY), both of which are bulk-sensitive methods.

DATA AVAILABILITY STATEMENT

Supporting research data has been deposited in the Oxford Research Archive and is available under this DOI:_____

EXTENDED DATA FIGURE LEGENDS

Extended Data Figure 1. Further Structural Characterisation of Pristine Materials Neutron Powder Diffraction data for (a) $Na_{0.75}[Li_{0.25}Mn_{0.75}]O_2$ and (b) $Na_{0.6}[Li_{0.2}Mn_{0.8}]O_2$ refined using the $P6_3/mmc$ space group, which excludes superstructure ordering. Rietveld refinement was performed using GSAS II software. Refinement parameters are given in the tables below. Inductively Coupled Plasma – Optical Emission Spectroscopy (ICP-OES) was used to confirm the chemical compositions.

Extended Data Figure 2. Diffraction Peaks Arising from Ribbon Superstructure Ordering in $Na_{0.6}[Li_{0.2}Mn_{0.8}]O_2$ (a) Powder X-ray Diffraction (PXRD) data for pristine $Na_{0.6}[Li_{0.2}Mn_{0.8}]O_2$ indexed using the P63/mmc space group which does not account for superstructure peaks arising from in-plane ordering in the TM layer. (b) Superstructure region of PXRD compared with computer generated diffraction patterns. Model crystal structures were prepared with different alignments of ribbon ordered layers. The only structure to match successfully all of the peaks is the P21/c space group. Structures are all viewed along the [010] direction.

Extended Data Figure 3. Operando Gas Evolution Analysis Operando Electrochemical Mass Spectometry (OEMS) collected on $Na_{0.6}[Li_{0.2}Mn_{0.8}]O_2$ at 10 mA g^{-1} between 2 and 4.5 V. No direct O_2 loss is observed. Only a very small quantity of CO_2 is released at 3.5 - 4.2 V characteristic of alkali carbonate decomposition, a small amount is released at 4.5 V due to direct electrolyte oxidation. Overall 0.005 moles of CO_2 per mole of active material were detected during charge compared with 0.4 moles of charge stored per mole of active material. Even if all of this CO_2 arose from O loss from the lattice, it would only constitute a very minimal contribution (0.02 moles of charge stored p.f.u.) or ~5% to the charge capacity observed.

Extended Data Figure 4. Manganese L-edge Spectra and Low Resolution RIXS for $Na_{0.6}[Li_{0.2}Mn_{0.8}]O_2$ (a) Electrochemical load curve for first cycle of $Na_{0.6}[Li_{0.2}Mn_{0.8}]O_2$ showing state of charge points selected for *ex situ* analysis (b) Manganese L-edge data collected in inverse Partial Fluorescence Yield (iPFY) mode show that $Na_{0.6}[Li_{0.2}Mn_{0.8}]O_2$ remains unchanging at Mn^{4+} throughout the charge and dicharge cycle. Standards shown

below are MnO (+2), Mn_2O_3 (+3) and Li_2MnO_3 (+4). (c) Low resolution RIXS spectra collected at BL27SU, Spring8 synchrotron, Japan, at 531 eV excitation energy show a new feature at an emission energy of ~523 eV corresponding to new hole states formed on O and an increase in the elastic peak intensity (labelled with arrows). These new features disappear on discharge indicating O reduction and the spectra are almost superimposable with those collected for the pristine material. The intensity of both features appears much less pronounced than the O redox features measured on honeycomb ordered O-redox materials.

Extended Data Figure 5. Two-phase Evolution in Li Environment in $Na_{0.6}[Li_{0.2}Mn_{0.8}]O_2$ *Ex situ* ^{6}Li MAS NMR spectra for $Na_{0.6}[Li_{0.2}Mn_{0.8}]O_2$ collected at different states of charge illustrate the two-phase nature of the charge-discharge plateau. Negligible change in the lithium environment is observed below 3.5 V in the single phase region. Arrows indicate the unique isotropic chemical shifts for Li.

Extended Data Figure 6. Further EM imaging showing Retention of Ribbon and Loss of Honeycomb Ordering ADF-STEM images showing further spatial investigation of the charged and discharged samples of (a) $Na_{0.6}[Li_{0.2}Mn_{0.8}]O_2$ with ribbon ordering and (b) $Na_{0.75}[Li_{0.25}Mn_{0.75}]O_2$ with honeycomb ordering. A further image showing $Na_{0.6}[Li_{0.2}Mn_{0.8}]O_2$ after 10 charge/discharge cycles is also included.

Extended Data Figure 7. Energetic Stability Afforded by O_2 Formation and Computed Discharge Voltage (a) Energetics of possible configurations of desodiated structural models for $Na_{0.0}Li_{0.25}Mn_{0.75}O_2$. The models considered are: P2-type stacking with Li in the TM layer (P2/Li_{TM}); O2-type stacking with Li in the TM layer (O2/Li_{TM}); O2-type staking with Li in the AM layer (O2/Li_{AL}); and O2-type stacking with Li in the AM layer and with in-plane Mn disorder (O2/Li_{AL}/Mn_{dis}). In the last case, various Mn disorder configurations were investigated corrsponding to the different crosses, the lowest energy structure is pictured (ab-plane) and posseses clusters of vacancies and Mn-bound O_2 with an O-O bond length of 1.2 Å corresponding to molecular O_2. For simplicity, the energies of the optimized models are plotted relative to the energy of the model P2/Li_{TM}, the energy of which was set to zero. The yellow curve is a guide to the eye to indicate the models with the lowest total energies. (b) Calculated lattice parameters for pristine, charged, and discharged $Na_{0.75}Li_{0.25}Mn_{0.75}O_2$. They are compared with experimental data. The deviation between theory and experiment is also reported. (c) and (d) Structural models used to compute the change in energy and average voltage for $Na_{0.75}Li_{0.25}Mn_{0.75}O_2$ and $Na_{0.6}Li_{0.2}Mn_{0.8}O_2$ respectively. Discharge reactions and calculated voltages are given in (iii). Purple – Mn, Green – Li, Yellow – Na.

Extended Data Figure 8. Ribbon Ordering Identified in P3-type $Na_{0.6}[Li_{0.2}Mn_{0.8}]O_2$ PXRD data for P3-type $Na_{0.6}[Li_{0.2}Mn_{0.6}]O_2$ reproduced with permission from Du et al. *Energy Environ. Sci.* 9, 2575, (2016). Below are calculated diffraction patterns for the P3 structure with and without ribbon ordering of Li and Mn in the TM layer. Vertical dotted lines show positions of superstructure peaks. The structure used for the calculation of the ribbon ordered P3-type $Na_{0.6}Li_{0.2}Mn_{0.6}O_2$ diffraction pattern is shown to the right and possesses an offset arrangement of ordered layers.

Extended Data Figure 9. Evolution of Electrochemical Behaviour over Resting and Cycling (a) Electrochemical load curves for $Na_{0.6}[Li_{0.2}Mn_{0.8}]O_2$ electrodes charged to 4.5 V at a rate of 10 mA g^{-1}, then rested at open circuit voltage (OCV) for varying amounts of time before discharge at 10 mA g^{-1}. (b) and (c) Electrochemical load curves for ribbon ordered $Na_{0.6}[Li_{0.2}Mn_{0.8}]O_2$ and honecycomb ordered $Na_{0.75}[Li_{0.25}Mn_{0.75}]O_2$ electrodes respectively, cycled between 2.0 V and 4.5 V at a rate of 10 mA g^{-1}. First cycle blue.

Extended Data Figure 10. Gradual Loss of Ribbon Superstructure Ordering from Diffraction *Ex situ* PXRD patterns for $Na_{0.6}[Li_{0.2}Mn_{0.8}]O_2$ in the discharged state (2.0 V) after 1, 10 and 20 charge/discharge cycles (between 2.0 V and 4.5 V at 10 mA g^{-1}). Peaks arising from the periodicity uniquely along the c-axis remain sharp upon cycling (indexed as 002 and 004 according to the P63/mmc space group without superstructure), whereas all other peaks, especially the 010 and 110, which are unique to ordering within the ab plane, broaden and reduce in intensity as the ribbon superstrucure is lost on cycling.

Additional References

36. Massiot, D. et al. Modelling one- and two-dimensional solid-state NMR spectra. Magn. Reson. Chem. 40, 70–76 (2002).

37. Jones, L. et al. Smart Align—a new tool for robust non-rigid registration of scanning microscope data. Adv. Struct. Chem. Imaging 1, 8 (2015).

38. Cococcioni, M. & de Gironcoli, S. Linear response approach to the calculation of the effective interaction parameters in the LDA + U method. Phys. Rev. B 71, 035105 (2005).

39. Giannozzi, P. et al. QUANTUM ESPRESSO: a modular and open-source software project for quantum simulations of materials. J. Phys. Condens. Matter 21, 395502 (2009).

40. Perdew, J. P., Burke, K. & Ernzerhof, M. Generalized Gradient Approximation Made Simple. Phys. Rev. Lett. 77, 3865–3868 (1996).

41. Blöchl, P. E. Projector augmented-wave method. Phys. Rev. B 50, 17953–17979 (1994).

42. Lee, D. H., Xu, J. & Meng, Y. S. An advanced cathode for Na-ion batteries with high rate and excellent structural stability. Phys. Chem. Chem. Phys. 15, 3304 (2013).

43. Schlipf, M. & Gygi, F. Optimization algorithm for the generation of ONCV pseudopotentials. Comput. Phys. Commun. 196, 36–44 (2015).

44. Aydinol, M. K., Kohan, A. F., Ceder, G., Cho, K. & Joannopoulos, J. Ab initio study of lithium intercalation in metal oxides and metal dichalcogenides. Phys. Rev. B 56, 1354–1365 (1997).

45. Aydinol, M. K., Kohan, A. F. & Ceder, G. Ab initio calculation of the intercalation voltage of lithium-transition-metal oxide electrodes for rechargeable batteries. J. Power Sources 68, 664–668 (1997).

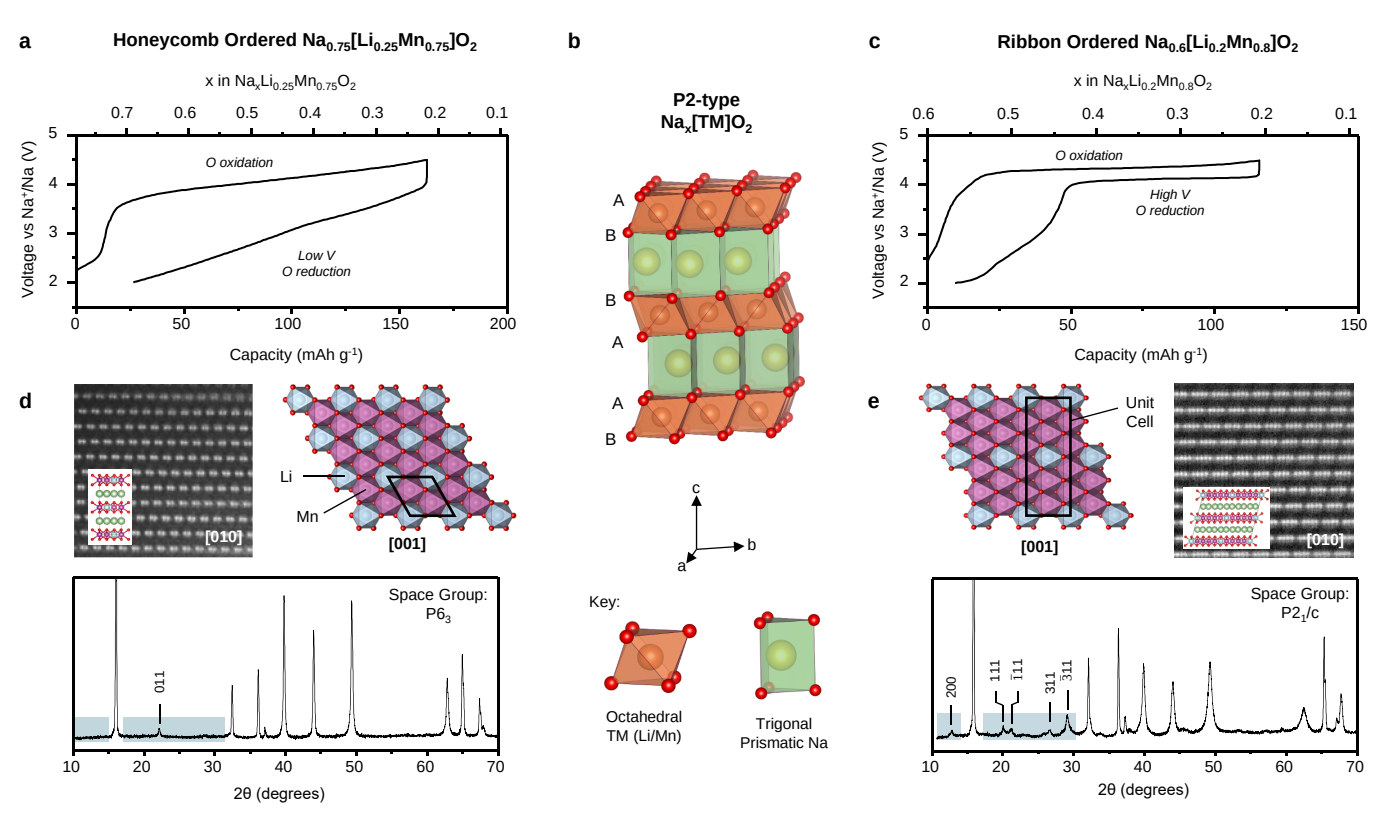
a
Honeycomb Ordered $Na_{0.75}[Li_{0.25}Mn_{0.75}]O_2$
x in $Na_xLi_{0.25}Mn_{0.75}O_2$
0.7 0.6 0.5 0.4 0.3 0.2 0.1
Voltage vs Na^+/Na (V)
O oxidation
Low V
O reduction
Capacity (mAh g^{-1})
b
P2-type
$Na_x[TM]O_2$
A
B
B
A
A
B
c
Ribbon Ordered $Na_{0.6}[Li_{0.2}Mn_{0.8}]O_2$
x in $Na_xLi_{0.2}Mn_{0.8}O_2$
0.6 0.5 0.4 0.3 0.2 0.1
Voltage vs Na^+/Na (V)
O oxidation
High V
O reduction
Capacity (mAh g^{-1})
d
[010]
Li
Mn
[001]
Space Group:
$P6_3$
011
2θ (degrees)
c
b
a
Key:
Octahedral
TM (Li/Mn)
Trigonal
Prismatic Na
e
Unit
Cell
[001]
[010]
Space Group:
$P2_1/c$
200
111
$\bar{1}11$
311
$\bar{3}11$
2θ (degrees)

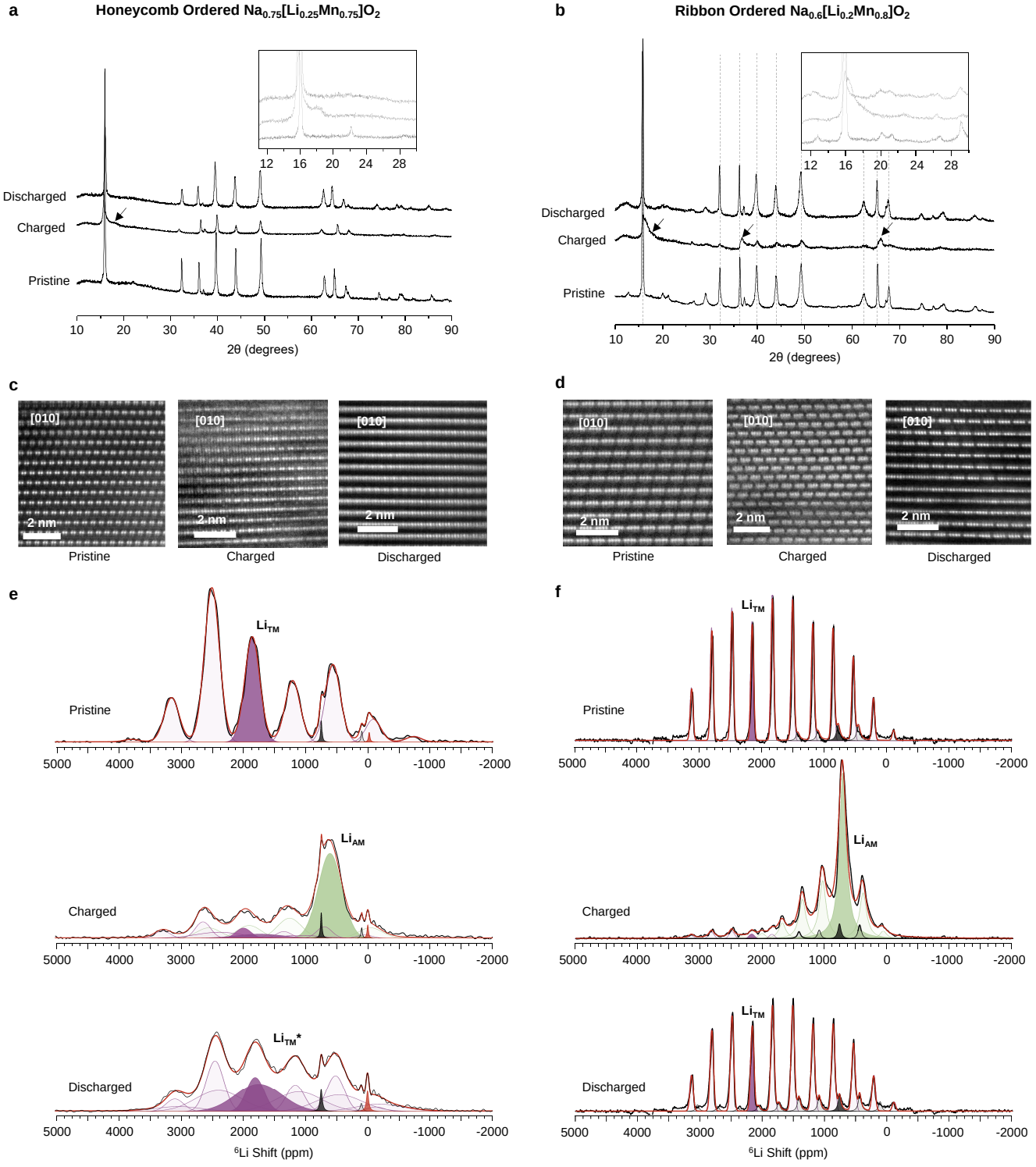
a
Honeycomb Ordered $Na_{0.75}[Li_{0.25}Mn_{0.75}]O_2$
Discharged
Charged
Pristine
2θ (degrees)
b
Ribbon Ordered $Na_{0.6}[Li_{0.2}Mn_{0.8}]O_2$
Discharged
Charged
Pristine
2θ (degrees)
c
[010]
2 nm
Pristine
Charged
Discharged
d
[010]
2 nm
Pristine
Charged
Discharged
e
Li_{TM}
Pristine
Li_{AM}
Charged
Li_{TM}*
Discharged
^{6}Li Shift (ppm)
f
Li_{TM}
Pristine
Li_{AM}
Charged
Li_{TM}
Discharged
^{6}Li Shift (ppm)

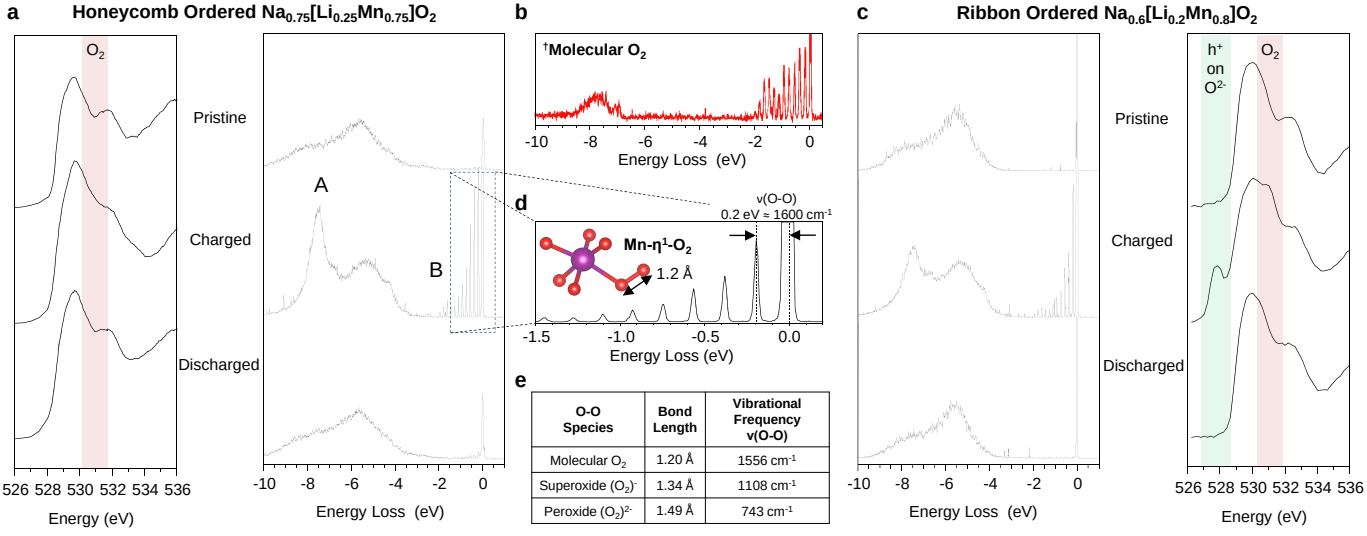

O-O Species	Bond Length	Vibrational Frequency v(O-O)
Molecular O_2	1.20 Å	1556 cm^{-1}
Superoxide $(O_2)^-$	1.34 Å	1108 cm^{-1}
Peroxide $(O_2)^{2-}$	1.49 Å	743 cm^{-1}

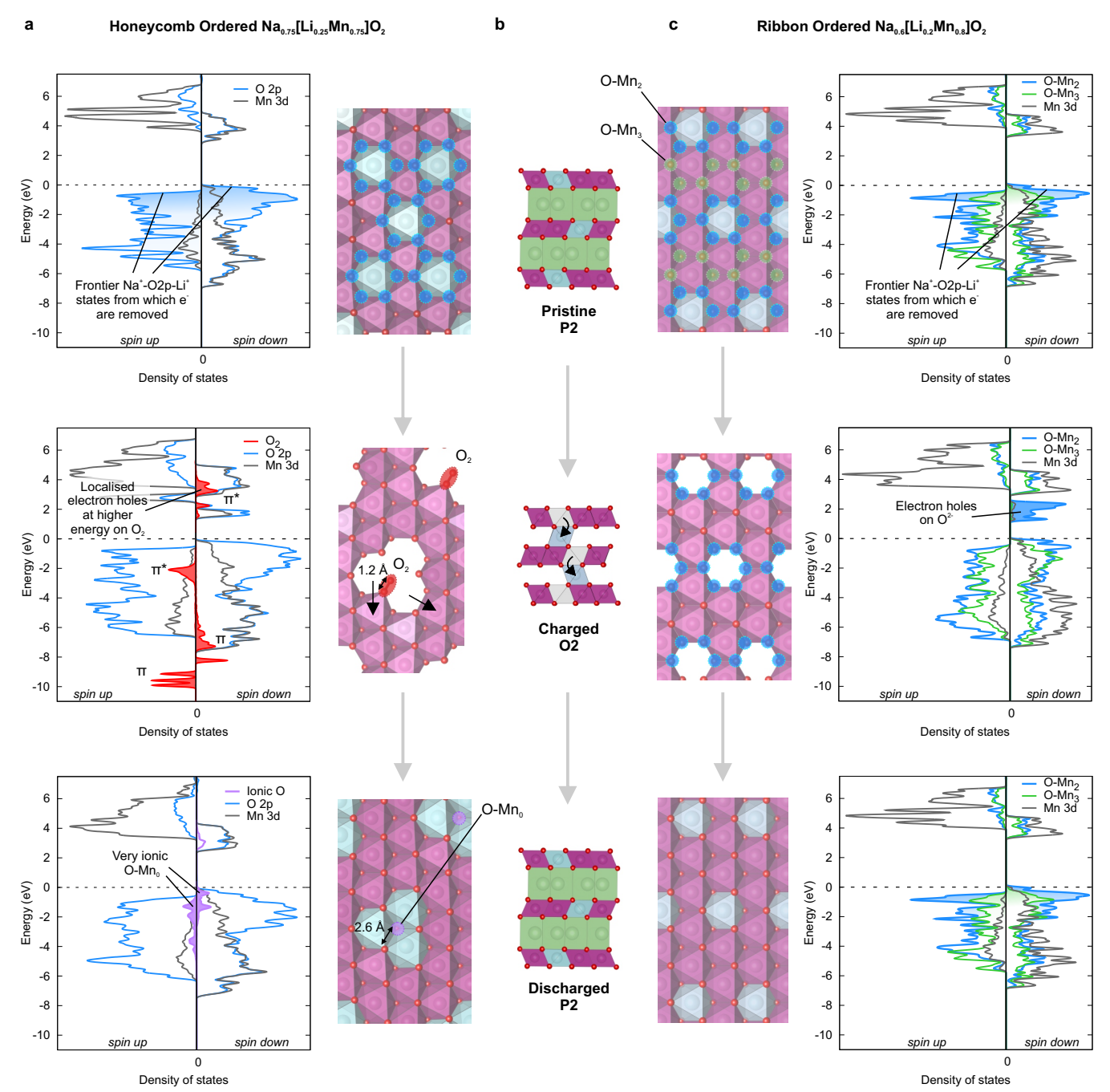
a
Honeycomb Ordered $Na_{0.75}[Li_{0.25}Mn_{0.75}]O_2$
b
c
Ribbon Ordered $Na_{0.6}[Li_{0.2}Mn_{0.8}]O_2$
O 2p
Mn 3d
Energy (eV)
Density of states
spin up
spin down
Frontier Na^+-O2p-Li^+ states from which e^- are removed
O-Mn$_2$
O-Mn$_3$
Pristine P2
O_2
Localised electron holes at higher energy on O_2
π*
π
1.2 Å
Charged O2
Electron holes on O^{2-}
Ionic O
Very ionic O-Mn$_0$
O-Mn$_0$
2.6 Å
Discharged P2

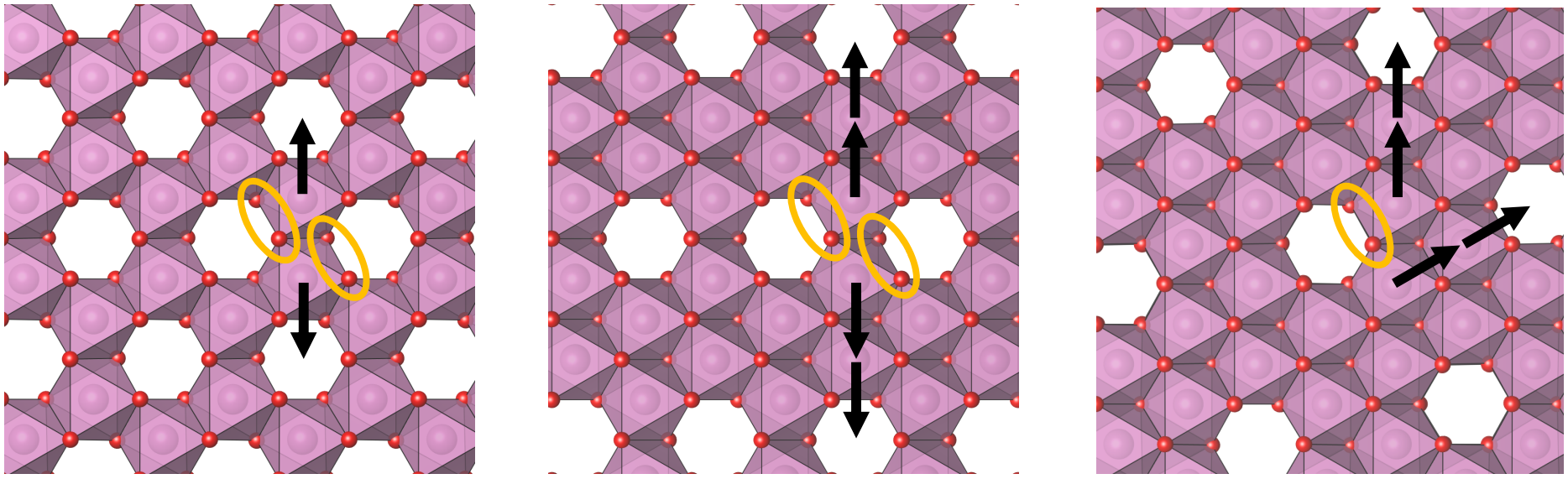
a
b
c
Honeycomb
□1/3TM2/3
P2-Na0.75Li0.25Mn0.75O2
Li1.2Ni0.2Mn0.6O2
Ribbon
□1/5TM4/5
P2-Na0.6Li0.2Mn0.8O2
P3-Na0.6Li0.2Mn0.8O2
Mesh
□1/7TM6/7
Na2Mn3O7
Increasing superstructure stability